Progress In Electromagnetics Research C, Vol. 157, 119–128, 2025

PIER C

(Received 30 April 2025, Accepted 23 June 2025, Scheduled 7 July 2025)

# Integrated High-Isolation Dual-Band Power Amplifier with Ring-Coupled Bandstop Filter

Jingchang Nan, Hai Jiang*, and Wenjin Liu

*School of Electronics and Information Engineering, Liaoning Technical University, Huludao 125105, China*

**ABSTRACT:** This paper addresses the challenge of inter-band interference suppression in Dual-Band Power Amplifier (DBPA) by proposing a high-isolation dual-band power amplifier design integrated with a Ring-Coupled Bandstop Filter (RCBSF). Through a ring-coupled structure of main transmission lines and coupled branches, combined with the collaborative tuning of $\lambda/4$ open stubs and coupling capacitor, the design achieves low-loss transmission in the dual-frequency passbands of 1.5 GHz and 2.1 GHz, forms a suppression band of $\geq 20$ dB in the 1.6–2.0 GHz range, and realizes deep suppression of $> 40$ dB for second/third harmonics. The RCBSF is embedded into the output matching network of the power amplifier to form a dual-band power amplifier. Measured results show that the power-added efficiencies (PAEs) of the amplifier at 1.5 GHz and 2.1 GHz are 58% and 60%, respectively, with output powers of 38 dBm and 37 dBm, and gains of 15 dB and 14 dB, respectively. In non-target frequency bands, the PAE approaches 0%, and a suppression greater than 40 dB is achieved, verifying that the filter's high selectivity and compact layout enhance the performance of the dual-band power amplifier. This design achieves efficient power transmission and strong interference isolation, providing a cost-effective solution for multi-band communication systems.

## 1. INTRODUCTION

Currently, available spectrum resources are becoming increasingly scarce, while the demand for dual-band power amplifiers, which are essential in communication systems, continues to grow [1], with design innovations for dual-band power amplifiers being particularly prominent. To meet the requirements for efficient transmission and processing of signals across different frequency bands, wireless communication systems employing dual-band power amplifiers (DBPAs) for transmitting and receiving signals face significant design challenges [2]. Specifically, this work focuses on the 1.5 GHz and 2.1 GHz bands. These frequencies are pivotal for modern multi-standard wireless systems, as they cover L-band satellite communication services (around 1.5 GHz) and key terrestrial mobile communication bands such as 3G/4G/5G (UMTS/LTE Band 1 at 2.1 GHz). An amplifier operating across these bands is highly desirable for terminals requiring both satellite and terrestrial connectivity, such as in automotive or portable communication devices.

Several studies have proposed dual-band matching networks using multi-section transmission line circuits. For example, [3] proposed a shunt and series stub solution, while [4] introduced a three-section series transmission line solution. In [5], a Class-J power amplifier utilizing a lumped $\pi$-type output matching network was proposed to enhance efficiency and linearity. Some studies employ switches to select matching frequencies. Ref. [6] proposed a front-end architecture comprising two tunable single-band impedance tuners, with one tuner selected via a pair of switches to determine the operational frequency band. Ref. [7] presented a matching network design methodology based on high-pass filter (HPF) and low-pass filter (LPF) transmission line phase shifters. Ref. [8] utilized semiconductor switches on transmission line transformers (TLTs) to achieve frequency-dependent matching. Ref. [9] achieved 2.4 GHz or 5 GHz matching by incorporating two switched capacitors into a T-shaped matching network. In terms of reconfigurability, BST (Barium Strontium Titanate) film-based intelligent bias circuits exhibit unique advantages, offering a dielectric constant tuning range of 300%, enabling dynamic switching between dual bands at 1.8–2.5 GHz and 3.4–3.8 GHz, with switching time reduced to the 5 µs level [10]. Recent research combines Class-J architecture with Doherty topology, achieving a breakthrough power-added efficiency (PAE) of 78% in dual bands at 2.4 GHz and 5.8 GHz — a 22-percentage-point improvement over conventional broadband power amplifiers [11]. This design employs a 3D stacked $\pi$-type matching network to extend second-harmonic suppression to 55 dBc.

However, the aforementioned various existing dual-band or reconfigurable power amplifier design schemes still face some challenges in practical applications. Schemes based on transmission line matching networks [3, 12–14] often have complex structures, require high fabrication precision, and struggle to effectively suppress inter-band interference. Solutions using switches or tunable components [6, 15, 16], despite offering frequency reconfigurability, introduce additional insertion loss, non-linearity, or control complexity. High-order or three-dimensional integration methods [11], while achieving excellent performance, typically rely on expensive high-end substrates and complex manufacturing processes, making them unfavorable for low-cost promotion. Traditional filter integration

* Corresponding author: Hai Jiang (nibu9521@163.com).

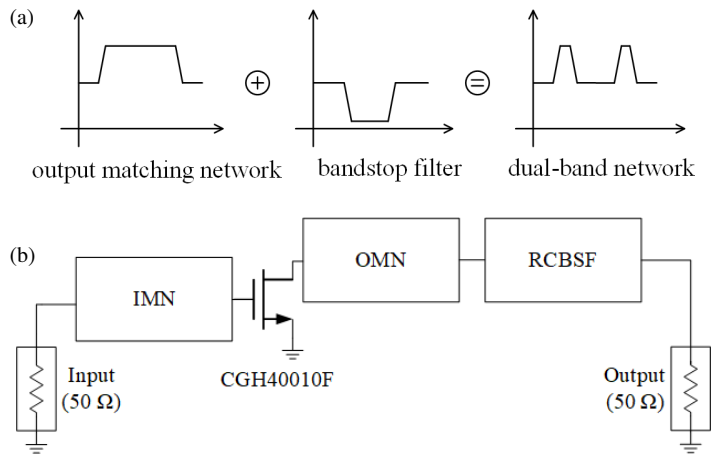


**FIGURE 1**. Conceptual overview of the dual-band power amplifier. (a) Design methodology of the dual-band system. (b) Block diagram of the overall DBPA architecture.

schemes may face challenges in the co-optimization between the filter and the power amplifier matching network, affecting the overall performance.

To address these issues, particularly achieving high-performance dual-band power amplifiers on low-cost FR4 substrates, this paper proposes an innovative design method by cleverly integrating a novel Ring-Coupled Bandstop Filter (RCBSF), offering a new solution for high-isolation dual-band power amplifier design. Detailed theoretical analysis and experimental validation demonstrate its performance, featuring passband frequencies at 1.5 GHz and 2.1 GHz, along with a strong attenuation stopband between 1.6 GHz and 2.0 GHz to eliminate unwanted signal interference that may degrade system performance. This design demonstrates excellent stopband characteristics, low insertion loss, and high selectivity across dual bands, effectively meeting the requirements of modern multi-band communication systems.

## 2. DUAL-BAND PA STRUCTURE

To achieve efficient amplification and spectral optimization of multi-band RF signals, this paper proposes a dual-band power amplifier (DBPA) architecture based on a coupled-resonator structural design. The design methodology, illustrated in Fig. 1(a), involves forming a composite dual-band network by cascading a dual-band output matching network with a bandstop filter [17].

To provide a clearer architectural view, the overall block diagram of the proposed DBPA is presented in Fig. 1(b). The architecture consists of an Input Matching Network (IMN), a Cree CGH40010F GaN HEMT serving as the active device, and an integrated output network. The output network is the core of this design, comprising a dual-band Output Matching Network (OMN) immediately followed by the proposed Ring-Coupled Bandstop Filter (RCBSF). The IMN is responsible for transforming the 50 Ω source impedance to the optimal input impedance of the transistor. The OMN and the RCBSF work in synergy to achieve two objectives simultaneously: first, to transform the 50 Ω load impedance to the optimal load impedances required by the transistor at the two passband frequencies (1.5 GHz and 2.1 GHz) for high efficiency and second, to provide strong signal suppression in the stopband (1.6–2.0 GHz) to ensure high inter-band isolation.

The dual-band power amplifier designed in this paper targets 1.5 GHz and 2.1 GHz operation, incorporating a drain-side output matching network (OMN) to ensure optimal impedance matching across the designated frequency ranges. To determine the optimal output matching impedance for the power amplifier (PA), Fig. 2 presents Smith chart trajectories of power contours and power-added efficiency (PAE) contours obtained through load-pull analysis at the target frequencies of 1.5 GHz and 2.1 GHz. The design objective of the output matching network is to transform the 50 Ω load impedance to the optimal impedance required by the power amplifier device at its output port for 1.5 GHz and 2.1 GHz (corresponding to the optimal load impedance region near the center of the power contours shown in Fig. 2, which yield high PAE and $P_{\text{out}}$). Load-pull analysis in the design identified the matching point best suited for balancing the performance across both operating frequencies. For a dual-band PA, an ideal output matching network should achieve optimal power transfer and high efficiency at

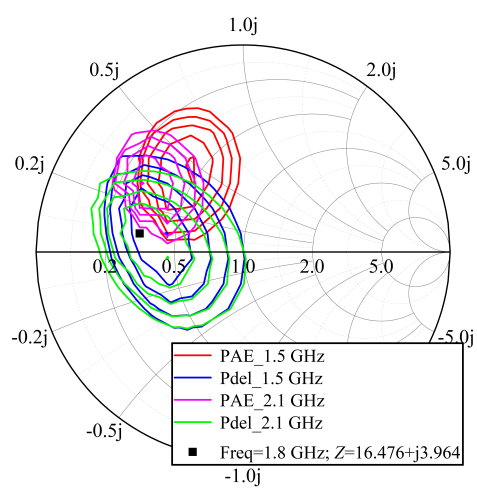


**FIGURE 2**. Smith chart trajectories at 1.5 GHz and 2.1 GHz.

the target frequencies. Additionally, to achieve high isolation in the non-target bands (1.6–2.0 GHz), the network must exhibit high impedance within this frequency range. Load-pull analysis in this design revealed an impedance point at 1.8 GHz ($Z = 16.476 + j3.964$), situated near the high-power/PAE regions of 1.5 GHz and 2.1 GHz, and this impedance characteristic is highly beneficial for the suppression provided by the subsequent RCBSF. Thus, the output matching network aims to transform the load impedance (50 Ω) to the optimal operating impedances at 1.5 GHz and 2.1 GHz, while also accounting for the 1.8 GHz impedance characteristics by appropriately selecting the matching structure and parameters to facilitate suppression by the RCBSF. Conjugate matching at the two frequency points is achieved via symmetrical transformations in an L-type matching network, adjusted through transmission line length and width parameters.

To effectively realize this high-impedance characteristic in the non-target band (1.6–2.0 GHz) and further suppress interband interference, a specially designed Ring-Coupled Bandstop Filter (RCBSF) is integrated into the system. The detailed theory and design of this filter will be elaborated in the following section.

## 3. RING COUPLED BANDSTOP FILTER

### 3.1. Theory of Ring Coupled Bandstop Filter

For dual-band power amplifiers, ensuring that effective isolation between the two frequency bands is critical. To suppress interference in the 1.6–2.0 GHz band and improve output signal purity, a ring-coupled bandstop filter (RCBSF) was designed to attenuate mid-band signals. The RCBSF employs an open-stub resonator configuration, operating on the principle of generating high impedance through resonant elements within a specific frequency band, thereby strongly suppressing signals in that band while minimally affecting other frequencies.

The RCBSF design must overcome multiple technical challenges, including achieving a wide and deep stopband, optimizing insertion loss and return loss in both low- and high-frequency passbands, and minimizing device size while maintaining performance. In this design, these key factors have been fully considered to ensure efficiency and practicality [18].

The RCBSF employs a ring-coupled structure, utilizing a main transmission line (TL1 + TL2 + TL5) and a coupled branch (TL3 + TL4) to achieve bandstop functionality, with its equivalent circuit model illustrated in Fig. 3.

In Fig. 3, TL1, TL2, and TL5 form the main signal path of the RCBSF. TL1 is designed for impedance matching with the preceding stage to minimize signal reflection and improve input return loss. For computational simplicity, TL1 uses a 50 Ω characteristic impedance ($Z_1$) and $\lambda/4$ electrical length ($\theta_1$). TL2 primarily governs passband performance, ensuring unimpeded transmission of 1.5 GHz and 2.1 GHz signals while suppressing unintended amplification of other frequencies, thereby maintaining RCBSF bandwidth and insertion loss. It features a $\lambda/8$ electrical length ($\theta_2$). TL5, an open-circuit stub, enhances resonant effects to increase stopband depth and isolation while optimizing overall matching characteristics. With $Z_5 = 50\,\Omega$

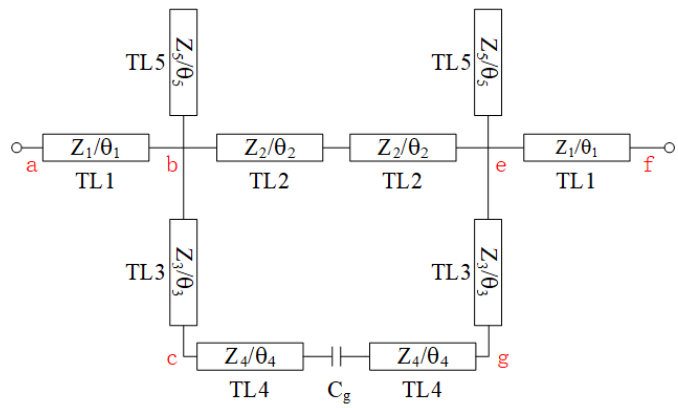


**FIGURE 3**. Equivalent circuit model of the RCBSF.

and $\theta_5 = \lambda/4$, it directly determines the stopband center frequency. TL3 and TL4 form a coupled resonator branch. TL3 generates resonance within the target stopband to reflect signals back to the input, reducing transmission and defining stopband position/depth. TL3 has a $\lambda/4$ electrical length ($\theta_3$). TL4, an open-circuit stub, forms a coupled-resonant structure with TL3 to strengthen stopband suppression. This coupling effect creates multiple theoretical transmission zeros within the target stopband, enabling precise harmonic suppression tuning. TL4 is designed with $\theta_4 = \lambda/4$. The impedance equations at each stage are calculated sequentially as follows:

$$Z_e = Z_1 \frac{Z_f + jZ_1 \tan\theta_1}{Z_1 + jZ_f \tan\theta_1} \tag{1}$$

$$Z_g = Z_3 \frac{Z_e + jZ_3 \tan\theta_3}{Z_3 + jZ_e \tan\theta_3} \tag{2}$$

Since the two TL4 ($Z_4/\theta_4$) sections contain a coupling capacitor $C_g$, the equivalent impedance of the coupled section must be calculated:

$$Z'_c = \left(\frac{2}{Z_{cg}} + j\omega C_g\right)^{-1} \tag{3}$$

where

$$Z_{cg} = Z_4 \frac{Z_g + jZ_4 \tan\theta_4}{Z_4 + jZ_4 \tan\theta_4} \tag{4}$$

and $\omega$ represents the angular frequency.

$$Z_c = Z_3 \frac{Z'_c + jZ_3 \tan\theta_3}{Z_3 + jZ'_c \tan\theta_3} \tag{5}$$

$$Z_b = Z_2 \frac{Z_c + jZ_2 \tan\theta_2}{Z_2 + jZ_c \tan\theta_2} \tag{6}$$

$$Z_a = Z_1 \frac{Z_b + jZ_1 \tan\theta_1}{Z_1 + jZ_b \tan\theta_1} \tag{7}$$

Based on Fig. 3 and the preceding impedance analysis, the entire filter can be divided into three cascade sections: input TL1 (nodes a to b), intermediate network (nodes b to e), and

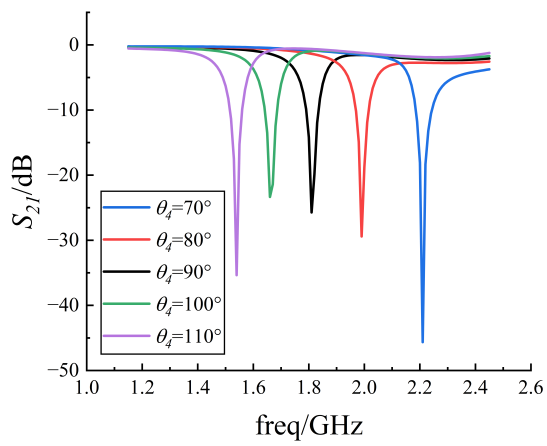


**FIGURE 4**. Simulated $S_{21}$ comparison for different electrical lengths $\theta_4$.

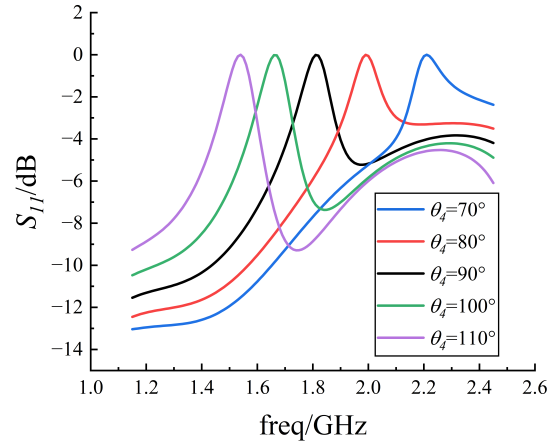


**FIGURE 5**. Simulated $S_{11}$ comparison for different electrical lengths $\theta_4$.

output TL1 (Nodes e to f). Let the transmission matrices of these three sections be denoted as $M_1$, $M_{\text{be}}$, and $M_3$. The total transmission matrix $M_{\text{total}}$ is then the product of these matrices:

$$M_{\text{total}} = \begin{bmatrix} A_{\text{total}} & B_{\text{total}} \\ C_{\text{total}} & D_{\text{total}} \end{bmatrix} = M_1 \times M_{\text{be}} \times M_3 \tag{8}$$

The $ABCD$ matrix for an ideal transmission line with characteristic impedance $Z$ and electrical length $\theta$ is given by:

$$M_{\text{TL}}(Z,\theta) = \begin{bmatrix} \cos\theta & jZ\sin\theta \\ j\dfrac{\sin\theta}{Z} & \cos\theta \end{bmatrix} \tag{9}$$

Therefore, $M_1 = M_3 = M_{\text{TL1}}$. To combine the parallel networks between nodes b and e (TL2, TL5, TL3 + TL4), we need to convert their individual $ABCD$ matrices ($M_{\text{TL2}}$, $M_{\text{TL5}}$, $M_{\text{TL34}}$) into Admittance ($Y$) matrices, and then sum the $Y$ matrices. The conversion formula from an $ABCD$ matrix to a $Y$ matrix is:

$$Y = \begin{bmatrix} Y_{11} & Y_{12} \\ Y_{21} & Y_{22} \end{bmatrix} = \frac{1}{B}\begin{bmatrix} D & -(AB-BC) \\ -1 & A \end{bmatrix} \tag{10}$$

Then the total admittance matrix $Y_{\text{be}}$ of the intermediate network (b-e) is:

$$Y_{\text{be}} = Y_{\text{TL2}} + Y_{\text{TL5}} + Y_{\text{TL34}} \tag{11}$$

Finally, convert the total admittance matrix $Y_{\text{be}}$ back into the $ABCD$ matrix $M_{\text{be}}$:

$$M_{\text{be}} = \begin{bmatrix} A & B \\ C & D \end{bmatrix} = \frac{1}{Y_{21}}\begin{bmatrix} -Y_{22} & -(Y_{11}Y_{22}-Y_{12}Y_{21}) \\ -1 & -Y_{11} \end{bmatrix} \tag{12}$$

For a system reference impedance $Z_0 = 50\,\Omega$, the scattering parameter $S_{11}$ and $S_{21}$ of the filter can be calculated from the elements of the $M_{\text{total}}$ matrix:

$$S_{11} = \frac{A_{\text{total}}Z_0 + B_{\text{total}} - C_{\text{total}}Z_0^2 - D_{\text{total}}Z_0}{A_{\text{total}}Z_0 + B_{\text{total}} + C_{\text{total}}Z_0^2 + D_{\text{total}}Z_0} \tag{13}$$

$$S_{21} = \frac{2Z_0}{A_{\text{total}}Z_0 + B_{\text{total}} + C_{\text{total}}Z_0^2 + D_{\text{total}}Z_0} \tag{14}$$

By substituting the structural parameters of the RCBSF into the derived Eqs. (13) and (14), the theoretical frequency response ($S_{11}$ and $S_{21}$) can be calculated. These equations, based on an ideal transmission line model, are crucial for providing initial design parameters and a fundamental understanding of the filter's behavior.

However, to account for real-world physical effects such as coupling between nonadjacent lines, parasitic effects, and microstrip discontinuities (e.g., bends and junctions), a full-wave electromagnetic (EM) simulation is necessary for accurate analysis and final optimization. Therefore, the subsequent performance analyzed in this paper, including the parametric studies shown in Figs. 4 and 5, is based on these more precise results of EM simulation obtained from advanced design system (ADS), which inherently validate and refine the initial theoretical design.

Compared to conventional bandstop filters [3, 4, 9, 19], the proposed RCBSF exhibits significant advantages in transmission zero control, size optimization, and stopband depth. Traditional approaches rely on fixed-length transmission lines or discrete components for dual-band suppression, offering limited adjustability of zero locations and struggling to achieve multi-pole suppression across wide stopbands.

The RCBSF overcomes these limitations through the following design innovations:

1. Flexible Resonance and Zero-Point Tuning: The synergistic resonance between main transmission line TL5 and coupled branch TL3 + TL4, combined with coupling capacitor $C_g$ between TL4 sections, generates 2–3 transmission zeros in the target stopband. By adjusting the electrical length $\theta_4$ and the coupling gap of the coupled branch, the suppression depth at 1.8 GHz can exceed 25 dB, outperforming traditional solutions in zero-point adjustability.

2. Compact Ring Structure and Component Reuse: A coplanar ring layout is adopted, where TL3 is miniaturized via

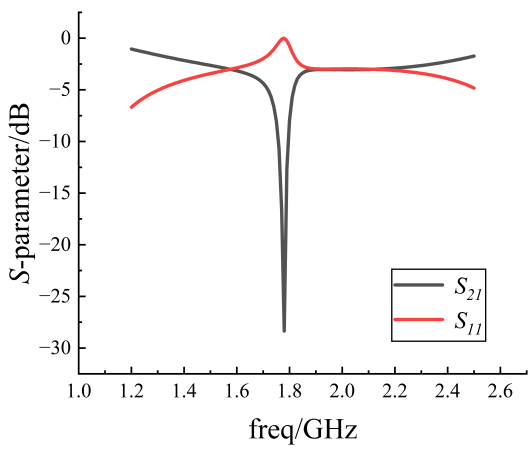


**FIGURE 6**. Simulated $S$-Parameters ($S_{11}$ and $S_{21}$) without TL5.

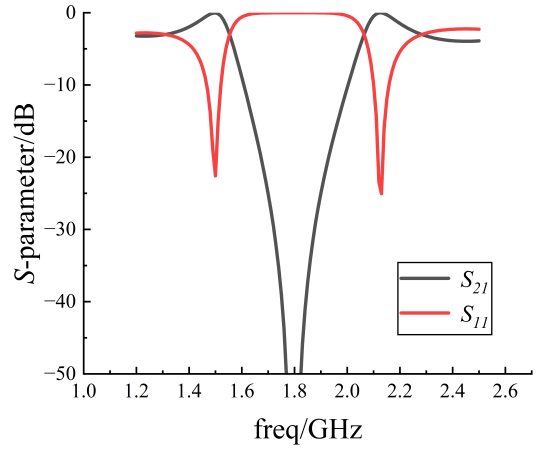


**FIGURE 7**. Simulated $S$-Parameters ($S_{11}$ and $S_{21}$) with TL5.

bent microstrip lines, resulting in an overall RCBSF footprint of 40 mm × 45 mm.

3. Deep Stopband and Broadband Suppression: The incorporation of TL5 enhances stopband depth and bandwidth, while coupling capacitor $C_g$ provides additional suppression exceeding 40 dB at second and third harmonics.

### 3.2. Simulation of Ring Coupled Bandstop Filter

The design process of the RCBSF typically combines theoretical analysis and electromagnetic simulation. First, based on the target passbands (1.5 GHz, 2.1 GHz) and stopband (1.6–2.0 GHz) requirements, the initial electrical lengths and characteristic impedances of each RCBSF transmission line section are determined using transmission line theory or filter synthesis methods. Then, these initial parameters are input into microwave circuit simulation software to build the physical model of the RCBSF and perform electromagnetic field simulation. Through iterative optimization of physical dimension parameters such as the length, width, and coupling gap of each transmission line section, the filter's $S$-parameter performance is finely tuned until it meets the design requirements for low passband insertion loss, high stopband suppression depth, and steep transition bands. Particularly on cost-sensitive FR4 substrates, due to process variations in dielectric constant and loss tangent, the performance of the RCBSF is quite sensitive to physical dimension deviations. In the design, robustness is ensured through parameter sweeping and sensitivity analysis, while the ring-coupled structure achieves a higher equivalent quality factor (Q value) in the high stopband frequency range, which is crucial for achieving sharp frequency response and high selectivity.

In the equivalent circuit model, TL3 and TL4 function as a series resonant network. At $\theta_4 = 90°$ ($\lambda/4$), the equivalent impedance at 1.8 GHz approaches infinity, creating a strong stopband. Fig. 4 presents simulated $S_{21}$ transmission coefficients of the RCBSF versus frequency under varying electrical lengths $\theta_4$ of the coupled branch. As $\theta_4$ increases progressively, both the position and depth of the attenuation peak in the target band undergo marked changes, demonstrating the critical influence of the coupled resonator's electrical length on stopband center frequency and bandwidth. At $\theta_4 = 70°$, the primary attenuation peak occurs near 2.2 GHz with $> 40$ dB suppression, while attenuation at $\sim 1.6$ GHz remains shallow. When $\theta_4 = 90°$, suppression depth at 1.8 GHz exceeds $-25$ dB. Further increasing $\theta_4$ to 100° and 110° shifts the stopband toward lower frequencies.

Figure 5 shows the simulated reflection coefficient $S_{11}$ versus frequency. When the RCBSF forms a strong stopband at a specific frequency, a pronounced reflection peak emerges, correlating with the deep $S_{21}$ attenuation in Fig. 4. As $\theta_4$ increases, the stopband center and suppression depth shift accordingly, accompanied by corresponding displacements of $S_{11}$ peaks. Thus, tuning $\theta_4$ in the coupled resonator branch enables frequency-reconfigurable high-selectivity deep attenuation while maintaining passband matching, achieving either enhanced suppression depth or broader stopband coverage.

The incorporation of TL5 extends the RCBSF's stopband range while maintaining sufficient suppression depth, thereby enhancing isolation performance. Figs. 6 and 7 compare the frequency responses of RCBSF with/without TL5. In Fig. 6 (without TL5), only a single distinct notch exists near 1.8 GHz, while transmission characteristics at 1.5 GHz and 2.1 GHz remain suboptimal, failing dual-passband requirements. In Fig. 7 (with TL5), $S_{21}$ approaches 0 dB at 1.5 GHz and 2.1 GHz with $S_{11} < -20$ dB, indicating efficient signal transmission, while a wider/deeper suppression band (1.6–2.0 GHz) is formed. This confirms that TL5 integration enables RCBSF to achieve low-loss transmission at target frequencies (1.5/2.1 GHz) while strengthening midband suppression and isolation, effectively rejecting 1.6–2.0 GHz interference to meet design specifications.

Beyond the stopband resonance formed by TL3 and TL4, the coupling effect between TL4s further enhances suppression. The electric field coupling between TL4s creates an equivalent capacitance $C_g$, which introduces additional capacitive reactance into the coupled resonator branch. Combined with transmission line inductance, this forms an LC resonant network, generating transmission zeros at higher-order harmonic frequencies. This resonance drives the equivalent impedance

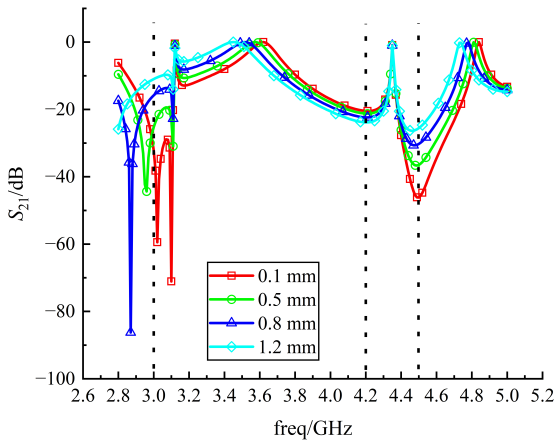


**FIGURE 8**. Effect of coupling gap width on harmonic suppression ($S_{21}$).

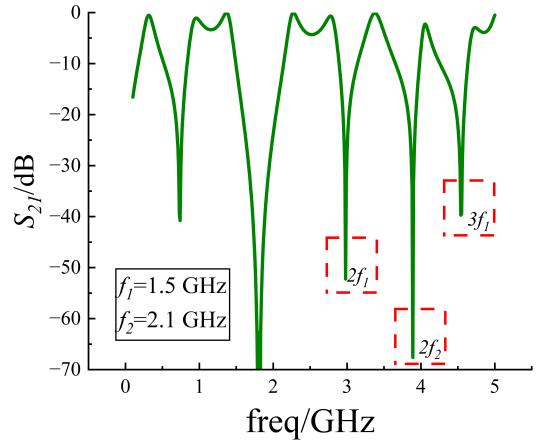


**FIGURE 9**. Simulated suppression effect of 2nd and 3rd harmonics.

toward infinity, forcing the harmonic signals to reflect back to the input port, thereby achieving deep suppression. Unlike traditional filters relying solely on fundamental resonance, the incorporation of $C_g$ empowers the RCBSF with active harmonic suppression capabilities, rather than depending purely on transmission line attenuation.

To validate the critical role of the coupling capacitance $C_g$, a parametric analysis was performed by varying the physical gap width between the TL4 sections. As shown in Fig. 8, the width of the coupling gap has a significant impact on the position and depth of the harmonic suppression notches. As the gap decreases from 1.2 mm to 0.1 mm, the transmission zero around 4.5 GHz becomes significantly deeper, achieving over 50 dB of suppression. Similarly, the notch around 3 GHz is also strongly influenced. This analysis demonstrates that $C_g$ provides a crucial degree of freedom for precise harmonic tuning.

As shown in Fig. 9, when the fundamental frequency is $f_1 = 1.5$ GHz, suppression depths at $2f_1$ and $3f_1$ exceed 50 dB and 40 dB, respectively. $C_g$ and TL4 form a series resonance at $2f_1$, resulting in a sharp decline in $S_{21}$. At $2f_2$ of the $f_2 = 2.1$ GHz fundamental frequency, the suppression depth exceeds 65 dB, meeting harmonic suppression requirements and effectively restraining gain.

## 4. LAYOUT DESIGN AND MEASUREMENT

### 4.1. Physical Production

Building on the theoretical framework proposed earlier, this work employs ADS software to successfully design a high-efficiency dual-band power amplifier operating at 1.5 GHz and 2.1 GHz. System-level simulations validate key performance metrics — including gain, efficiency, and output power — at both target frequencies, confirming the theoretical design's validity. For experimental validation, FR4 substrate ($\epsilon_r = 4.4$, $\tan\delta = 0.017$) was selected as the dielectric material. This choice balances cost-effectiveness and engineering feasibility: its widespread industrial adoption, machinability, and high permittivity enable compact microstrip layouts aligned with miniaturization goals. Measured results demonstrate that optimized matching networks and RCBSF achieve target gain and efficiency, proving the architecture's effectiveness on commercial-grade substrates. A Cree CGH40010F GaN HEMT device was implemented as the core power transistor for hardware realization.

Figure 10 illustrates the schematic diagram of the overall dual-band power amplifier structure. The labels in parentheses within the RCBSF section correspond to the transmission line elements in the equivalent circuit model shown in Fig. 3. Within this structure, the Input Matching Network (IMN) is responsible for impedance matching at the input terminal. The main task of the IMN is to transform the 50 Ω source impedance to the optimal input impedance of the GaN HEMT device at the working frequencies of 1.5 GHz and 2.1 GHz (these points are typically related to achieving desired power gain, efficiency, and linearity). Similar to the output matching network, the dual-band IMN can be implemented using multi-section transmission lines or lumped element networks. In practical design, the input impedance of the transistor usually exhibits capacitive behavior at high frequencies. This design employs a simplified L-type matching network structure [20] to achieve good input return loss at the two target frequencies by optimizing microstrip line length and width or capacitance/inductance values. The design of the IMN also needs to consider the power amplifier's stability, preventing oscillations within the operating bands or out-of-band. This can be achieved by adding appropriate resistive or absorbing networks (e.g., a resistor in parallel with an inductor) at the transistor's input terminal, improving out-of-band stability while maintaining in-band matching. The Gate Bias Circuit and Drain Bias Circuit provide stable DC bias voltage and current for the GaN HEMT device, setting its operating mode. Specifically, the drain bias voltage ($V_D$) and gate bias voltage ($V_G$) are set to 28 V and $-2.9$ V, respectively. Component parameters are detailed in Table 1. These values were determined through a standard design methodology involving load-pull analysis and matching network synthesis using Smith charts. The fundamental theory and calculation procedures for these techniques are well established in standard microwave engineering literature, such as [21].

As discussed in Section 3.2, the gap between the two TL4s was optimized through parameterized simulation and finally set

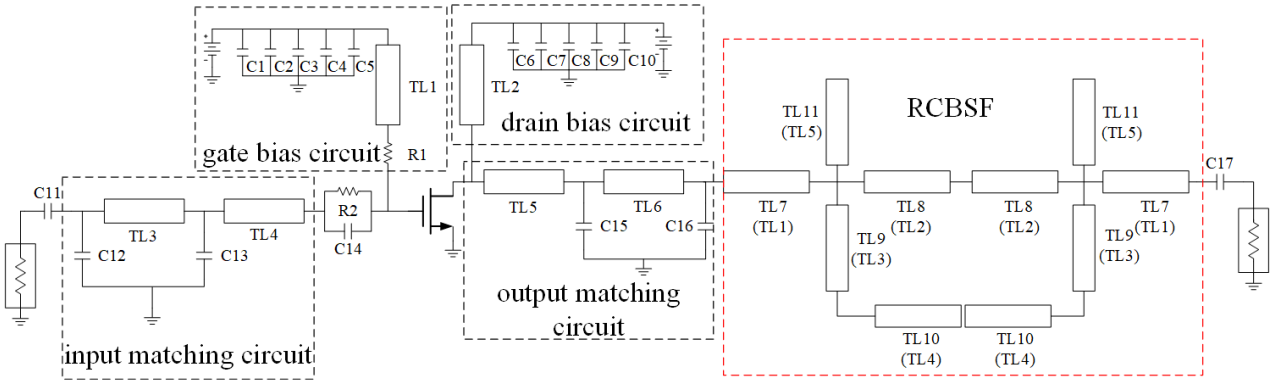


**FIGURE 10**. Schematic diagram of the overall dual-band power amplifier structure.

**TABLE 1**. Detailed parameters of all components in DBPA.

| Component | Value | Component | Value |
|---|---|---|---|
| C1, C10 | 10 µF | C12 | 1.6 pF |
| C2, C9 | 10 nF | C13 | 4.6 pF |
| C3, C8 | 1 nF | C14 | 6 pF |
| C4, C7 | 100 pF | C15 | 5 pF |
| C5, C6 | 15 pF | C16 | 2.9 pF |
| C11, C17 | 15 pF | R1 | 50 Ω |
| R2 | 7 Ω | TL6 | 6.3/1.8 |
| TL1 | 22/1.8 | TL7 | 13.7/3.3 |
| TL2 | 22/1.8 | TL8 | 12.4/6.6 |
| TL3 | 17.7/5.2 | TL9 | 17/1.5 |
| TL4 | 1.4/1.8 | TL10 | 14/6 |
| TL5 | 2.7/1.2 | TL11 | 22.5/1.8 |

to 0.43 mm in the layout. In Table 1, the format for microstrip line dimensions is length/width (mm).

Compact layout was achieved through meandered microstrip lines, with the physical prototype shown in Fig. 11. The overall size of the fabricated dual-band power amplifier is 60 mm × 100 mm. The overall circuit layout design is implemented on a low-cost FR4 substrate, balancing compact size and manufacturability. Microstrip line bending (such as mitered or rounded corners) is widely used to reduce transmission line size [22], especially in the ring structure and connecting lines of the RCBSF. In the layout design, the effects of bending on the microstrip line's electrical performance must be considered and corrected through simulation. To reduce the parasitic effects of on-board components, particularly the parasitic inductance of surface-mount capacitors and resistors, the pad design also needs optimization. For example, using multiple vias to connect to the ground plane can effectively reduce ground inductance. Furthermore, sufficient spacing between components and transmission lines is necessary to avoid unwanted coupling or potential arcing issues. The layout also needs to consider the isolation between DC bias lines and radio frequency (RF) signal lines; bias networks, typically composed of choke inductors and bypass capacitors, are commonly used to introduce DC voltage while suppressing RF signal leakage. A well-designed layout is essential for reducing spurious radiation, improving circuit isolation, and ensuring consistency between measured performance and simulation results.

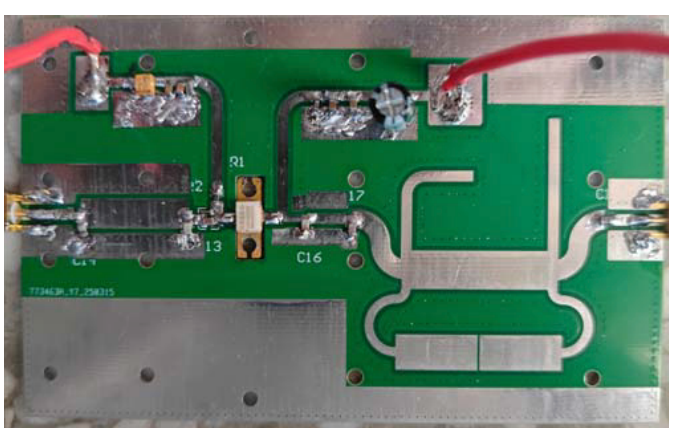


**FIGURE 11**. Physical photograph of the overall dual-band power amplifier.

### 4.2. Simulation and Experimental Measurement

Small-signal $S$-parameter simulations and experimental results of the dual-band power amplifier are shown in Fig. 12. The small-signal $S$-parameters were measured using a Ceyear 3674H vector network analyzer (VNA), which has a measurement frequency range of 10 MHz to 50 GHz. Results indicate that $S_{21}$ achieves high values at 1.5 GHz and 2.1 GHz, while $S_{11}$ remains below −10 dB at both frequencies, confirming excellent matching characteristics. Additionally, $S_{21}$ decreases significantly in non-target bands while $S_{11}$ increases, demonstrating effective suppression of out-of-band signals. The $S_{21}$ curve reveals gains of ∼ 15 dB at 1.5 GHz and ∼ 14 dB at 2.1 GHz. From the measured results, the 3 dB bandwidths of the two passbands can be determined. For the 1.5 GHz band, the amplifier exhibits a 3 dB fractional bandwidth (FBW) of approximately 6.7% (from 1.45 GHz to 1.55 GHz). For the 2.1 GHz band, the 3 dB FBW is approximately 4.8% (from 2.05 GHz to 2.15 GHz), demonstrating sufficient bandwidth for the targeted applications.

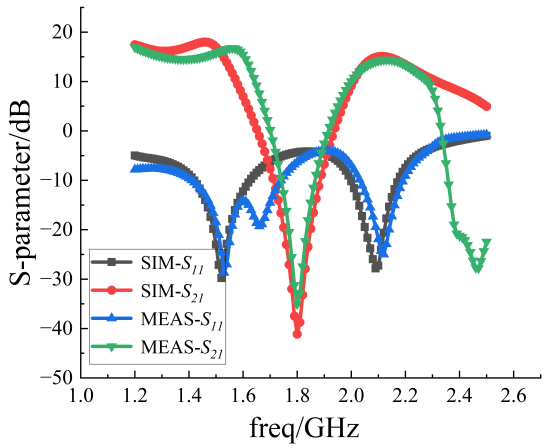


**FIGURE 12**. Small-signal $S$-Parameter simulation and experiment of the DBPA.

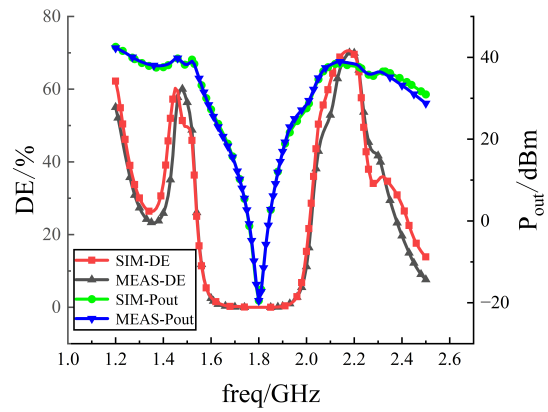


**FIGURE 13**. Simulated and measured Drain Efficiencies (DEs) and output powers ($P_{\text{out}}$) vs. frequency.

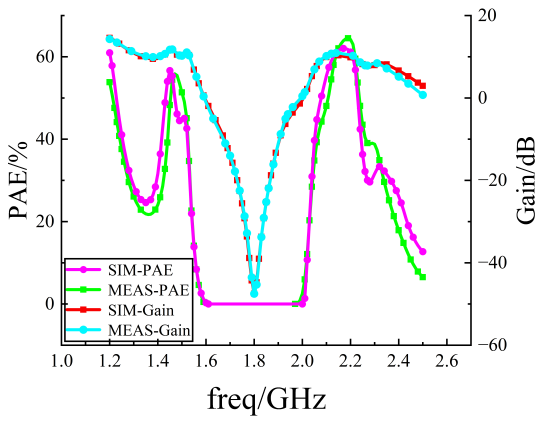


**FIGURE 14**. Simulated and measured Power-Added Efficiencies (PAEs) and gains vs. frequency.

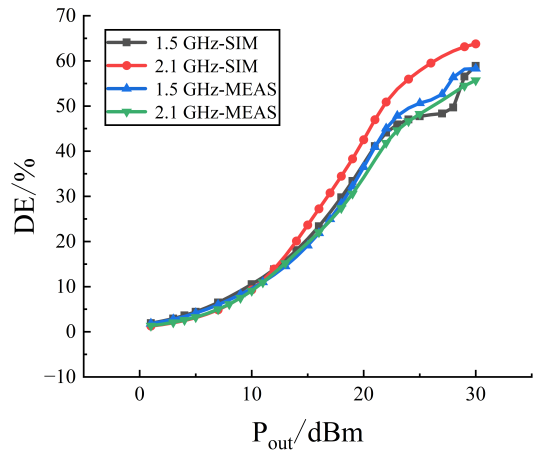


**FIGURE 15**. Simulated and measured Drain Efficiencies (DEs) vs. output power.

To further validate DBPA performance, Figs. 13 and 14 compare simulated and experimental efficiency metrics. Fig. 13 illustrates drain efficiency (DE) and output power ($P_{\text{out}}$) versus frequency. At target frequencies (1.5/2.1 GHz), measured DE values reached 60% and 65%, with corresponding $P_{\text{out}}$ of 38 dBm and 37 dBm, respectively. Fig. 14 compares simulated and measured PAEs and gains across frequencies. At 1.5/2.1 GHz, PAEs reached 58%/62% with gains of 15/14 dB. Between 1.6 and 2.0 GHz, DE/$P_{\text{out}}$ degraded sharply ($P_{\text{out}} <$ 0 dBm), with PAE $\approx$ 0% while the signal is suppressed by more than 40 dB, confirming strong mid-band suppression.

The measured PAE reduction stems from factors such as the equivalent series resistance (ESR) of surface-mount capacitors, the dielectric loss of the FR4 substrate, and radiation loss from the bent microstrip lines. Microstrip dimensional deviations and parasitic inductance introduced by soldering degrade the impedance matching accuracy, leading to an approximately 1 dB decrease in output power. The nonlinear gate-drain capacitance of the GaN device and DC supply ripple cause the saturation power point to shift, resulting in PAE discrepancies at high power levels. Despite these deviations between measured and simulated values caused by factors such as low-cost substrate process variations, component parasitic parameters, and testing environment, the main performance trends (including $S$-parameters, efficiency, and gain variation with frequency and power) demonstrate good consistency between simulation and experimental results. These consistent trends validate the correctness of the proposed architectural design and confirm stable and efficient operation at 1.5 GHz and 2.1 GHz.

Figures 15 and 16 compare simulated and measured DE/PAE versus $P_{\text{out}}$ for 1.5/2.1 GHz. As $P_{\text{out}}$ increases from 0 dBm to $>$ 30 dBm, peak DE reaches $\sim$ 60% (1.5 GHz) and 65% (2.1 GHz), while PAE peaks at $\sim$ 58% (1.5 GHz) and $\sim$ 62% (2.1 GHz). The agreement between simulated and measured trends demonstrates the PA's high efficiency and output capability across both 1.5 GHz and 2.1 GHz bands.

As Table 2 shows, compared to existing solutions, this work achieves $\geq$ 20 dB mid-band isolation via RCBSF integration, with 20% smaller footprint and 15 dB higher isolation than cascaded/switching approaches. This validates RCBSF's selectivity-PA co-design, offering a cost-effective multi-band solution.

**TABLE 2**. Performance comparison table of dual-band power amplifier.

| Ref. | Freq (GHz) | PAE (%) | Gain (dB) | Isolation degree (dB) | Size ($W \times L$ mm) |
|---|---|---|---|---|---|
| [11] | 1.95–2.4 /2.65–3.1 | 60 | 12 | $> 18$ | $50 \times 150$ |
| [17] | 2.1/2.91 | 75 | 12.5 | $> 20$ | $55 \times 151$ |
| [23] | 1.72/3.48 | 65 | 9.8 | - | $50 \times 75$ |
| [24] | 0.61/2.6 | 56.3 | - | $> 19$ | $121 \times 158$ |
| This work | 1.5/2.1 | 58/62 | 15/14 | $> 20$ | $60 \times 100$ |

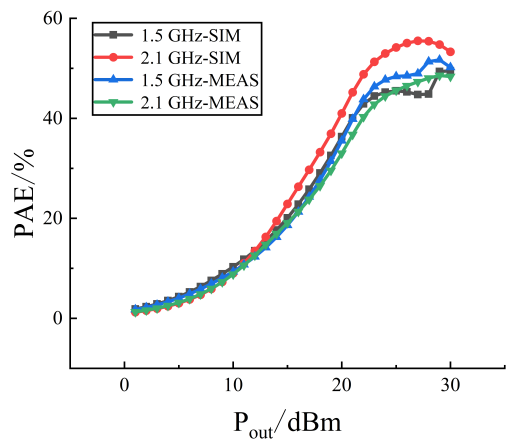


**FIGURE 16**. Simulated and measured Power-Added Efficiencies (PAEs) vs. output power.

## 5. CONCLUSION

This paper addresses the inter-band isolation challenge in dual-band systems by designing a resonant ring-coupled bandstop filter (RCBSF). Through synergistic tuning of open stubs and coupling capacitors, cascaded with a standard 50 Ω matching network, it achieves efficient amplification at 1.5/2.1 GHz and strong suppression in the 1.6–2.0 GHz band. Measured results validate the effectiveness of this design: At the two target frequency bands of 1.5 GHz and 2.1 GHz, the amplifier achieved power-added efficiencies of 58% and 60%, respectively, with output powers reaching 38 dBm and 37 dBm, and gains of 15 dB and 14 dB, respectively. In the non-target frequency band of 1.6–2.0 GHz, the gain was effectively suppressed, achieving an inter-band isolation of more than 40 dB. Simultaneously, the suppression of the second and third harmonics exceeded 40 dB for both bands. The core innovation lies in the high selectivity and compact layout of the RCBSF and its co-optimization with the power amplifier matching network, which effectively suppresses interference signals between the dual bands and improves system isolation. Its integration into a dual-band power amplifier validates its reliability and high performance in multi-band communication scenarios, offering a new approach for RF front-end miniaturization and cost-effective multi-band design. Future work could focus on achieving frequency reconfigurability by integrating tunable elements into the RCBSF structure, as well as applying linearization techniques to enhance the performance for modern wideband communication signals.

## ACKNOWLEDGEMENT

This work is supported by the National Natural Science Foundation of China (Grant No. 61971210).

## REFERENCES

[1] Liu, W., H. Wang, and J. Nan, "Design of reconfigurable dual-band radio frequency power amplifier based on PIN switch," *Chinese Journal of Radio Science*, Vol. 37, No. 1, 168–174, 2022.

[2] Nan, J., Q. Wang, Z. Li, and J. Pan, "Design of reconfigurable channel-selective power amplifier," *Chinese Journal of Radio Science*, Vol. 39, No. 3, 561–569, 2024.

[3] Maktoomi, M. A., M. Akbarpour, M. S. Hashmi, and F. M. Ghannouchi, "On the dual-frequency impedance/admittance characteristic of multisection commensurate transmission line," *IEEE Transactions on Circuits and Systems II: Express Briefs*, Vol. 64, No. 6, 665–669, Jun. 2017.

[4] Lin, Y.-S. and C.-H. Wei, "A novel miniature dual-band impedance matching network for frequency-dependent complex impedances," *IEEE Transactions on Microwave Theory and Techniques*, Vol. 68, No. 10, 4314–4326, Oct. 2020.

[5] Sridhar, N., C. Senthilpari, R. Mardeni, W. H. Yong, and T. Nandhakumar, "A low power, highly efficient, linear, enhanced wideband class-J mode power amplifier for 5G applications," *Scientific Reports*, Vol. 12, No. 1, 8101, 2022.

[6] Amin, H. Y., J. Chen, M. Berg, and A. Pärssinen, "Tunable front-end design with a dual-band antenna for small cellular devices," in *2019 13th European Conference on Antennas and Propagation (EuCAP)*, 1–5, Krakow, Poland, 2019.

[7] Yazdani, F. and R. R. Mansour, "Realization of dual-band matching networks using cascaded filters," in *2020 50th European Microwave Conference (EuMC)*, 727–730, Utrecht, Netherlands, 2021.

[8] Lee, J., J.-S. Paek, and S. Hong, "Millimeter-wave frequency reconfigurable dual-band CMOS power amplifier for 5G communication radios," *IEEE Transactions on Microwave Theory and Techniques*, Vol. 70, No. 1, 801–812, Jan. 2022.

[9] Liu, B., X. Quan, C. C. Boon, D. Khanna, P. Choi, and X. Yi, "Reconfigurable 2.4-/5-GHz dual-band transmitter front-end supporting 1024-QAM for WLAN 802.11 ax application in 40-nm CMOS," *IEEE Transactions on Microwave Theory and Techniques*, Vol. 68, No. 9, 4018–4030, Sep. 2020.

[10] Wen, H. and W. Feng, "Dual-band high-efficiency power amplifier based on harmonic control network," *Modern Applied Physics*, Vol. 14, 155–161, 2023.

[11] Zhang, Z., "Research and design of high-efficiency dual-band power amplifier," Master's thesis, South China University of

Technology, Guangzhou, Guangdong, China, 2023.

[12] Zhang, J., C. Yu, H. Li, and Y. Liu, "A novel dual-band power amplifier with integrated harmonic control based on dual transmission lines," *Microelectronics Journal*, Vol. 156, 106552, 2025.

[13] Boumalkha, M., M. Lahsaini, and M. E. H. Archidi, "Design of an efficiency-enhanced filtering power amplifier with a dual-band response and wide stopband," *AEU — International Journal of Electronics and Communications*, Vol. 183, 155366, 2024.

[14] Wang, J., Z. Dai, K. Zhong, G. Bai, C. Bi, M. Li, W. Shi, and J. Pang, "Design of a dual-band doherty power amplifier using single-loop network," *IEEE Transactions on Microwave Theory and Techniques*, Vol. 72, No. 10, 5818–5829, Oct. 2024.

[15] Liu, W., H. Dong, and J. Nan, "Design of class f reconfigurable power amplifiers," in *Journal of Physics: Conference Series*, Vol. 2761, No. 1, 012024, 2024.

[16] Xu, Y., X. Sun, X. Zhu, P.-L. Chi, and T. Yang, "A 2-18-GHz frequency-reconfigurable GaN power amplifier with more than 33added efficiency," *IEEE Transactions on Microwave Theory and Techniques*, Vol. 73, No. 4, 2320–2333, Apr. 2025.

[17] Zarghami, S. and M. Hayati, "A new design approach for dual-band power amplifiers based on dual-band HCC and bandpass filter," *Scientific Reports*, Vol. 14, No. 1, 1323, 2024.

[18] Wei, L.-Y., F.-C. Chen, and Z.-B. Zhang, "Design of dual-band power amplifier based on microstrip coupled-line bandstop filter," *AEU — International Journal of Electronics and Communications*, Vol. 185, 155450, 2024.

[19] Zuo, X. and L. Qin, "Three-line coupled-line narrowband bandstop filter with wide upper bandpass bandwidth," *AEU — International Journal of Electronics and Communications*, Vol. 140, 153936, 2021.

[20] Chen, Y., W. Choi, J. Shin, H. Jeon, S. Bae, S. Bin, S. Nam, Y. C. Choi, H. Kang, K.-Y. Lee, K. C. Hwang, and Y. Yang, "New compact load network for Doherty power amplifiers based on L-section matching network of the carrier amplifier and post-matching network," *IEEE Access*, Vol. 11, 66 478–66 487, 2023.

[21] Pozar, D. M., *Microwave Engineering: Theory and Techniques*, 4th ed., John Wiley & Sons, 2021.

[22] Chen, L.-P., L. Chi, C. Zhang, L.-F. Jiao, and M.-Y. Gui, "Analysis of microstrip line corner discontinuity based on RO4350B," *Electronic Quality*, Vol. 9, 94–97, Sep. 2023.

[23] Liu, J., C. Liu, Z. Shao, and W. Shi, "Design of a dual-band power amplifier over an octave bandwidth employing dual-band resonators," *International Journal of Numerical Modelling: Electronic Networks, Devices and Fields*, Vol. 37, No. 2, e3112, 2024.

[24] Yin, R. and W. Wang, "Design of high-efficiency dual band power amplifier based on GaN HEMT," in *Journal of Physics: Conference Series*, Vol. 2592, No. 1, 012049, 2023.